Angewandte Chemie
Eine Zeitschrift der Gesellschaft Deutscher Chemiker

Supporting Information

Lithium-Metal Anodes Working at 60 mA cm^{-2} and 60 mAh cm^{-2} through Nanoscale Lithium-Ion Adsorbing

Lei Ye[+], Meng Liao[+], Xiangran Cheng, Xufeng Zhou, Yang Zhao, Yibei Yang, Chengqiang Tang, Hao Sun, Yue Gao, Bingjie Wang, and Huisheng Peng**

ange_202106047_sm_miscellaneous_information.pdf

Supporting Information

1. Synthesis of graphene quantum dots

Graphene quantum dots, composed of nanoscale graphene domains in the core and abundant oxygen, nitrogen, and sulfur functional groups on the surface, were synthesized through a hydrothermal process based on polycondensation mechanism. Citric acid (0.21 g, 1 mmol) and thiourea (0.46 g, 3 mmol) were first dissolved into 10 mL deionized water under continuous stirring to obtain a clear solution. The solution was then decanted into a Teflon-lined stainless-steel hydrothermal reactor, which was tightly sealed and heated for 4 h at 160 ℃ in an electric oven. The graphene cores of graphene quantum dots were obtained by self-assembly and dehydrolysis of citric acid molecules into nanosheets due to their inter-molecular hydrogen bonds. Abundant carboxyl- and hydroxyl-groups remained as terminal groups. The bifunctional thiourea molecules then reacted with the end groups, further combining more citric acid molecules to form short polymer chains containing high contents of oxygen, nitrogen, and sulfur elements. After cooling to room temperature, the solution was alkalized by adding 1 M NaOH until pH of 6 and then purified by dialysis (3.5 kDa cut-off) for 6 h. Graphene quantum dots were obtained after freeze-drying for 24 h, and stored in an argon-filled glovebox (H_2O < 0.1 ppm, O_2 < 0.1 ppm) for further use.

2. Preparation of LAL/Li and LAL/Cu electrodes

A strongly polar solvent composed of mixed dimethyl sulfoxide and acetonitrile (0.75/1, *v*/*v*) was used to disperse the powder of graphene quantum dots. LAL/Li and LAL/Cu electrodes were prepared by a facile spin-coating method through iterating the spin-coating process for three times at 1000 $r \cdot s^{-1}$ and 60 s. The obtained LAL/Li electrode showed a smooth morphology similar to the bare Li electrode in both optical photographs and scanning electron microscopy (SEM) images (**Figures S8** and **S9**).

Abundant and uniformly distributed elements of C, O, N, and S were observed in the elemental mapping of the LAL/Li electrode, indicating successful incorporation of the LAL (**Figure S10**).

To optimize the thickness of LALs and achieve desirable electrochemical performances of LAL/Li electrodes, graphene quantum dot dispersions with increasing concentrations from 0.2 to 1.0 mg·mL^{-1} were used for fabrication and measurements of LALs. The LALs were first prepared on smooth silicon wafers for the evaluation of thickness through step profiler and AFM measurements. As shown in **Figure S7a**, the thickness of LAL increased from 20 to 150 nm upon the increase of dispersion concentration from 0.2 to 1.0 mg·mL^{-1}. The Li nucleation overpotential (μ_n) was first evaluated. The LAL/Cu electrode prepared with a quantum dot dispersion of 0.6 mg·mL^{-1} (~60 nm LAL) exhibited the lowest μ_n, which was much lower than that of the bare Cu electrode, *i.e.*, a concentration of 0 mg·mL^{-1} (**Figure S7b**). The reduced μ_n indicated a facilitated Li deposition in a more homogeneous manner at initial stages. Besides, the LAL/Cu electrode prepared with the quantum dot dispersion of 0.6 mg·mL^{-1} also demonstrated the highest Coulombic efficiency (CE) at the first Li plating/stripping cycle compared with other samples (**Figure S7c**). Therefore, the graphene quantum dot dispersion of 0.6 mg·mL^{-1} was adopted for the fabrication of LALs in this work and the resulting LAL thickness was ~60 nm (**Figure S12**). And the LAL showed a high Young's modulus of ~6.22 GPa determined by AFM analysis (**Figure S13**).

The LAL and Li metal could form chemical adhesion upon the incorporation process as indicated by X-ray photoelectron spectroscopy (XPS) depth profiling analysis. As shown in the high-resolution N 1s spectra, the peak assigned to -NH_2 could be observed within a depth of 40 nm and then gradually vanished at a depth of 60 nm (**Figure S14a**). Alternatively, the peak attributed to -NH- could still be observed at the depth of 60 nm, indicating the formation of -NH-Li bond on the LAL/Li electrode surface. Similarly, the intensity of the -OH peak could be observed within the depth of 50 nm and then

gradually vanished due to the reduction reaction with Li metal (**Figure S14b**). In addition, these results also confirmed the thickness of LAL spin-coated on Li metal surface was ~60 nm. To further confirm the chemical adhesion between the LAL and Li metal, synthesized graphene quantum dots were stirred with excessive Li pieces overnight and then collected for FTIR analysis. As a result, the broad absorption bands of -OH and -NH_2 (3000~3500 cm^{-1}) in pristine graphene quantum dots disappeared after the reaction with Li metal, verifying the conversion to -O-Li and -NH-Li bonds (**Figure S15**).

3. Electrochemical measurement of LAL based electrodes

To explore the cycling performances and interfacial properties, symmetric CR2032 coin cells were assembled using two LAL/Li or bare Li electrodes in an argon-filled glove box (H_2O < 0.1 ppm, O_2 < 0.1 ppm). 1 M lithium bis(trifluoromethanesulfonyl)imide (LiTFSI) dissolved in 1,3-dioxolane (DOL)/1,2-dimethoxyethane (DME) (1/1, *v*/*v*) with 1 *wt*% lithium nitrate ($LiNO_3$) was used as the electrolyte. Activated molecular sieves (4 A) were added for 24 h before use to remove the trace water. Celgard 2400 membranes were used as separators. Li plating/stripping was conducted under increasing galvanostatic current densities from 1 to 60 $mA \cdot cm^{-2}$ and areal capacities from 1 to 60 $mAh \cdot cm^{-2}$. Electrochemical impedance spectroscopy (EIS) tests were performed at the open-circuit potential over a frequency range of 10^{-2} to 10^{5} Hz and an amplitude at 5 mV. To test the CE, CR2032 coin cells were assembled as mentioned above employing the LAL/Cu or bare Cu as the working electrode and a Li plate as the counter/reference electrode. Metallic Li with an areal capacity of 1 $mAh \cdot cm^{-2}$ was first plated onto the working electrode at a current density of 1.0 $mA \cdot cm^{-2}$, and then stripped by charging to a cut-off voltage of 0.5 V (*vs* Li/Li^+). The CE was calculated as the ratio of Li stripped to that plated during each plating/stripping cycle.

4. Preparation of air cathodes for Li-air batteries

To prepare air cathodes of Li-air batteries, a spinnable CNT array was first synthesized through chemical vapor deposition process. Al_2O_3 (3 nm) and Fe (1.2 nm) were successively deposited on a silicon wafer as catalysts. Ethylene (90 sccm) was used as the carbon precursor, H_2 (30 sccm) was used as the reducing gas and Ar (400 sccm) was employed as the carrier gas. A temperature of 750 ℃ for 10 min was required to obtain a spinnable CNT array. The aligned CNT sheet with a thickness of ~20 nm was drawn from the spinnable CNT array and stacked for 20 layers to fabricate the air cathode of Li-air batteries. The as-prepared air cathode presented a geometric area of ~1 cm^2 and a mass load of 28.2 $\mu g \cdot cm^{-2}$.

5. Electrochemical measurements of Li-air batteries

Swagelok-type Li-air batteries were assembled for electrochemical measurements with the LAL/Li or bare Li anode, electrolyte, separator (glass fiber, Whatman GF/A) and aligned CNT cathode in an argon-filled glovebox. The electrolyte was prepared by dissolving 0.318 g lithium triflate (LiTF) and 0.0134 g lithium iodide (LiI) in 2.018 g tetraethylene glycol dimethyl ether (TEGDME). Activated molecular sieves (4 A) were added for 24 h before use to remove the trace water. The assembled Li-air batteries were directly tested in the ambient air with a fixed specific capacity of 500 $mAh \cdot g^{-1}$ at a current density of 1000 $mA \cdot g^{-1}$. The specific capacity (C) was defined as $C=(I \times t)/m$, where I, t, and m represented the discharge current, discharge time, and mass of the air electrode, respectively. EIS tests were implemented on a CHI 660D electrochemical workstation at a potential of 2.9 V over a frequency range of 10^{-2} to 10^5 Hz. The amplitude was 5 mV.

6. Density functional theory calculation method

All simulated computations were conducted by Generalized Gradient Approximation (GGA) based on density functional theory (DFT) with $DMol^3$ module and Perdew-Burke-Ernzerhof (PBE) exchange-correlation parameterization.[1, 2] Global orbital cutoff of 3.7 Å was adopted as the maximal value from all the cutoffs specific to each

element in this system. Interactions between ionic cores and valence electrons were described by all electron core treatments. The max ionic force and geometry optimization parameters of total energy convergence were 2×10^{-5} eV·Å^{-1} and 1×10^{-5} Ha, respectively. Zigzag monolayer graphene with various functional groups was employed as the fundamental models to manifest the structure of LAL. A four-layer 2 × 1 × 1 super cell was constructed to simulate the (*1 1 1*) crystal plane of Cu. Only the top two layers of atoms were set to fully relaxed and the bottom two layers were fixed. The binding energies of lithium atoms with the LAL or the Cu model were calculated according to:

$$E_b = E_{total} - E_{sub} - E_{Li}$$

E_b, E_{sub}, E_{Li} were the energies of the LAL model with Li atoms, LAL model, and lithium atoms in a lithium crystal, respectively.

7. COMSOL Multiphysics simulation method

All simulations were performed by COMSOL Multiphysics 5.4 with implemented finite element solver. The simulation of Li^+ distribution was conducted in 800×800 nm^2 half-cell electrodeposition system, employing an electrolyte of 1 M LiTFSI dissolved in DOL/DME (1/1, *v*/*v*) with 1 wt% $LiNO_3$. The reaction current for $Li^+ + e^- \rightarrow Li$ was 20 mA·cm^{-2}. Initial surface protuberances were introduced in the bare Li mode as Li dendrites to simplify the computation process.

8. Materials

Citric acid, thiourea, lithium triflate, and lithium iodide were acquired from Sigma-Aldrich. TEGDME was obtained from Sinopharm. The 1 M lithium bis(trifluoromethanesulfonyl)imide (LiTFSI) in 1,3-dioxolane (DOL)/1,2-dimethoxyethane (DME) (1/1, *v*/*v*) with 1 *wt*% lithium nitrate ($LiNO_3$) electrolyte and the 1 M Lithium hexafluorophosphate ($LiPF_6$) in ethylene carbonate (EC)/diethyl carbonate (DEC) (1/1, *v*/*v*) electrolyte were ordered from Shanghai Xiaoyuan Energy Co. Ltd. Cu foils were obtained from Shenzhen Kejing Star Technology Corporation. Li plate was purchased from China Energy Lithium Co. Ltd. The Celgard 2400 separator was obtained from Celgard Co. Ltd. The Whatman G/F A separator was from

Whatman Co. Ltd.

9. Characterization

LAL/Li and bare Li electrodes were disassembled from the CR2032 coin cells or Swagelok-type batteries, rinsed in solvent twice to remove residual electrolyte salt, and dried for 24 h in vacuum before further characterization. The morphology was characterized by scanning electron microscopy (SEM, Zeiss Gemini SEM500 FESEM operated at 1 kV; EDS Aztec X-Max Extreme EDS operated at 20 kV) and transmission electron microscopy (TEM, JEOL JEM-2100F operated at 200 kV). The chemical properties were characterized by Raman spectroscopy (Dilor LabRam-1B, He-Ne laser of 4 mW, excitation wavelength of 632.8 nm), X-ray diffraction (Bruker AXSD8), X-ray photoelectron spectroscopy (PHI5000C & PHI5300, Mg, 250 W, 14 kV), Fourier transform infrared spectrometer (Thermofisher, Nicolet 6700), and atomic force microscopy (Multimode 8). The electrochemical performances were obtained from an Arbin electrochemical station (MSTATS-10V/3A/32Ch) and CHI 660D electrochemical workstation. Photographs were taken by a digital camera (SONY A6000, Japan). The air-sensitive electrodes were transferred in an argon-filled sealed box into the chambers of testing instruments. For XRD analysis, samples were sealed in Kapton film to prevent side reactions in ambient air during testing.

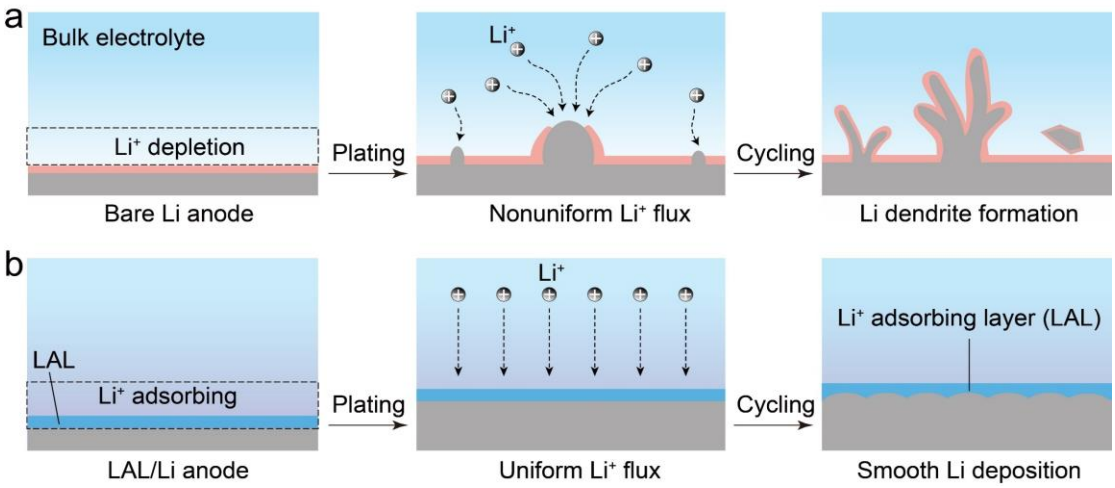

Figure S1. **(a)** and **(b)** Li plating/stripping behaviors for bare Li and LAL/Li anodes, respectively. In LAL/Li anodes, Li^+ ions were able to penetrate through the LAL during electrochemical deposition, leading to Li deposition beneath the LAL.

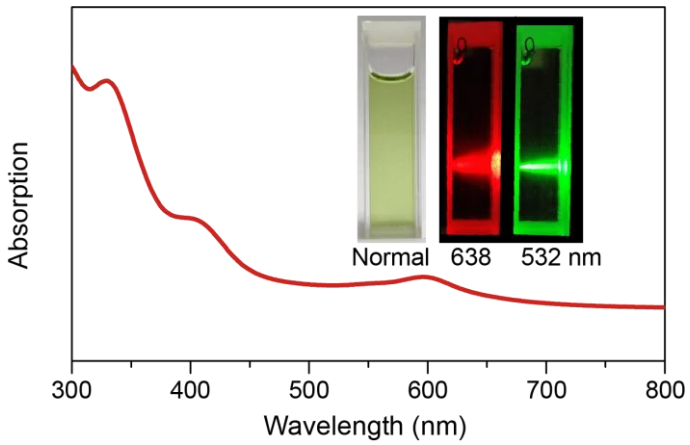

Figure S2. UV-vis absorption spectrum of the electronegative graphene quantum dots. The absorption bands at 337, 405, and 595 nm were attributed to quantum-sized graphene, C=O, and C=S bonds, respectively. Inset: optical images of the graphene quantum dots dispersion and its excited states at different wavelengths of light.

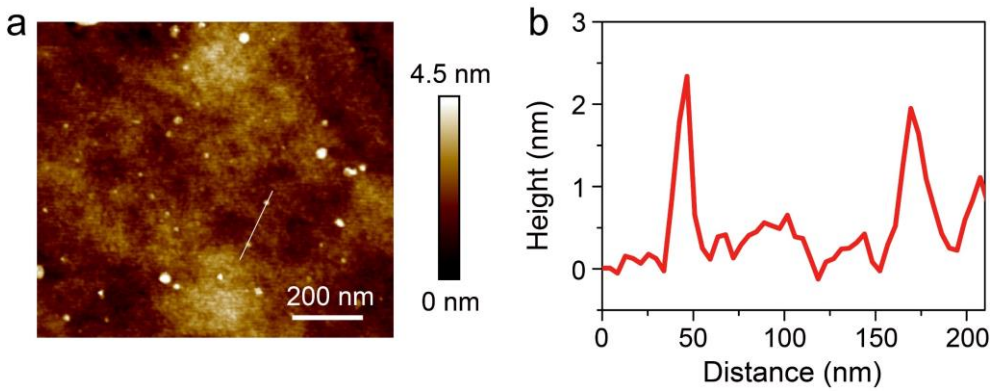

Figure S3. **(a)** AFM image of the graphene quantum dot on a silicon substrate. **(b)** The height profile along the line in **(a)**.

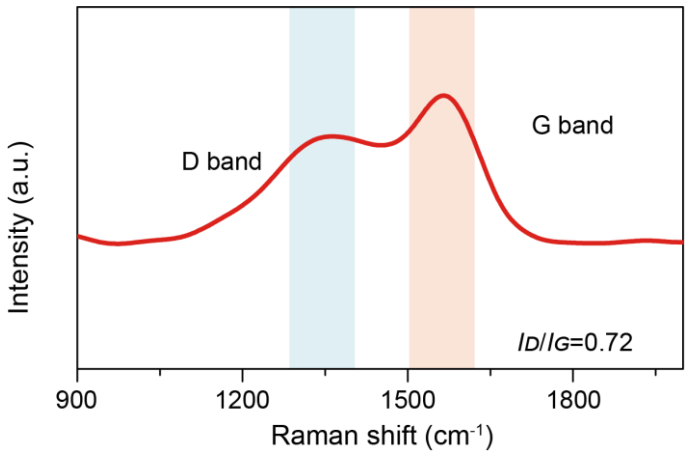

Figure S4. Raman spectrum of the graphene quantum dot powders. The crystalline (G) band at 1573 cm^{-1} could be assigned to the in-plane vibration of sp^2 carbon, indicating the presence of graphene phase.

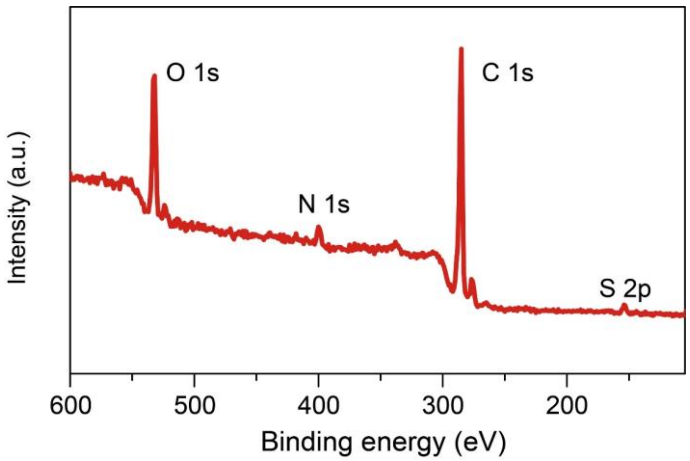

Figure S5. XPS spectra of the LAL.

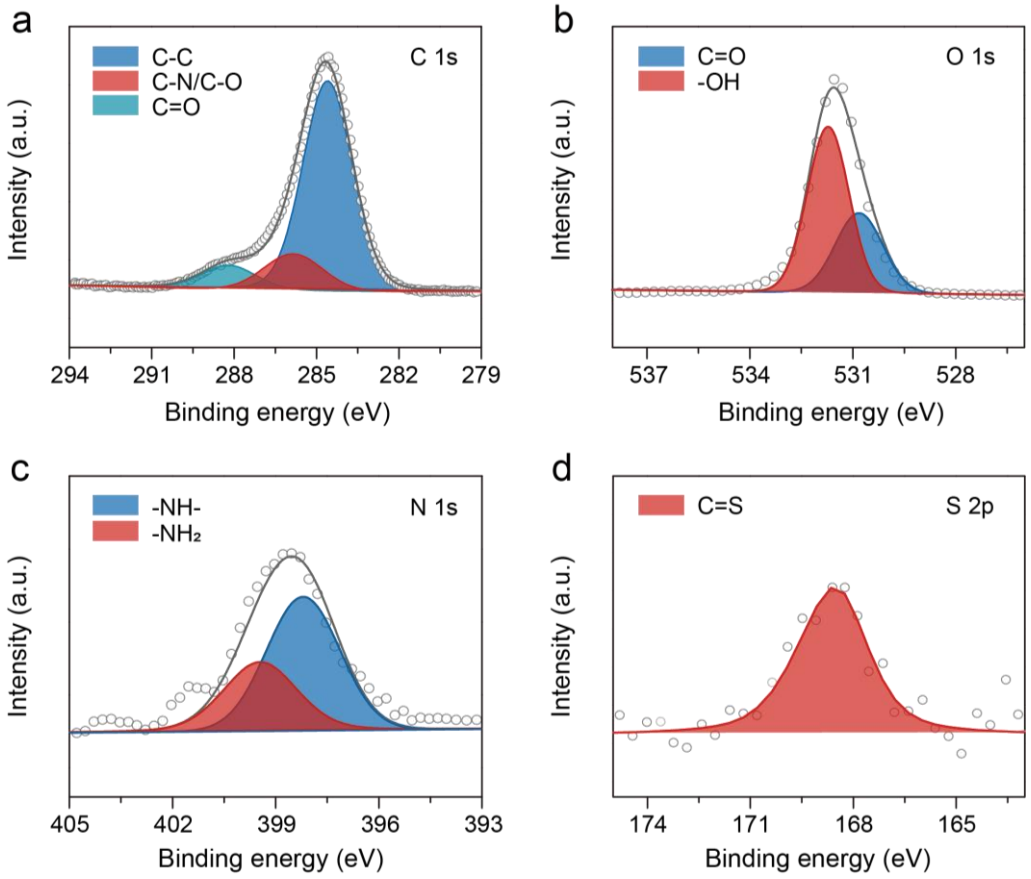

Figure S6. **(a)-(d)** High-resolution C 1s, O 1s, N 1s, and S 2p XPS spectra of the LAL, respectively. The binding energy values were all calibrated using the adventitious C 1s peak at 284.6 eV.

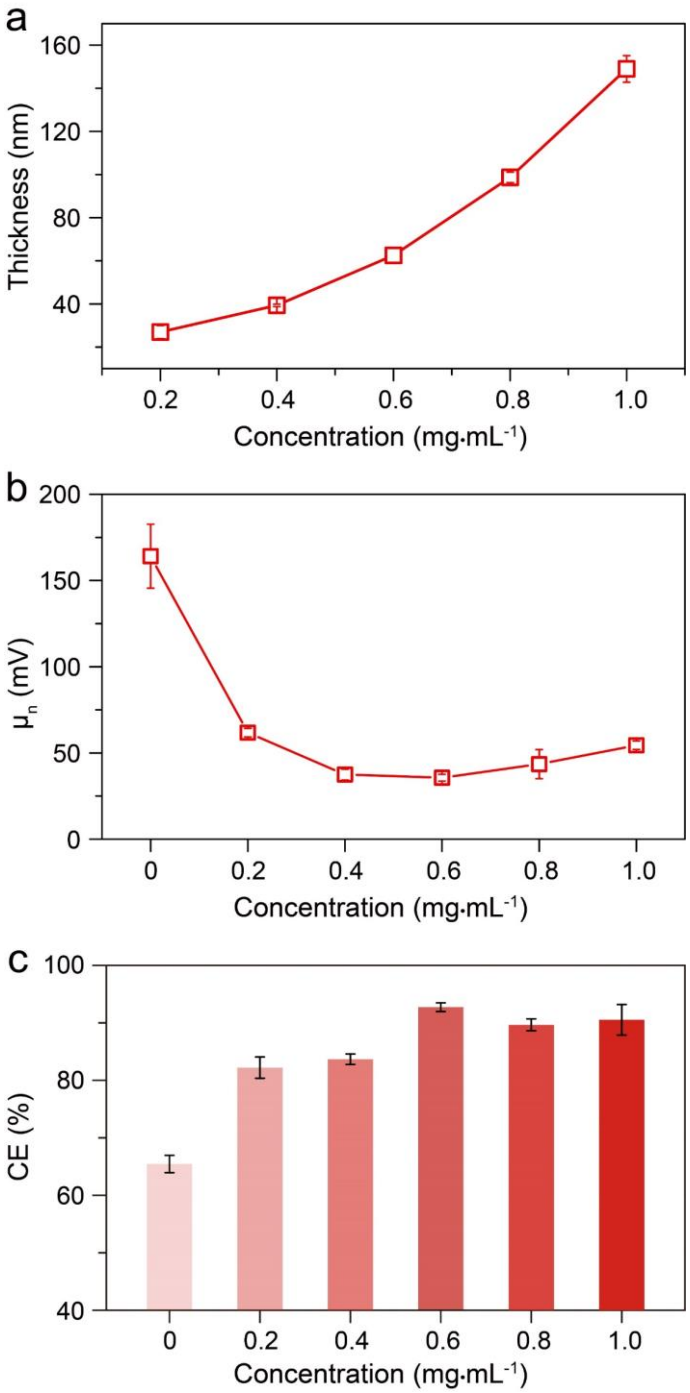

Figure S7. **(a)** The dependence of spin-coated LAL thickness on the adopted concentration of graphene quantum dots dispersion. To avoid potential influence from the wrinkles on electrode surface, the LALs were directly prepared on planar silicon wafer for the thickness measurement. **(b)** and **(c)** Nucleation overpotentials and initial CEs of Li||Cu batteries incorporated with LALs constructed by varying concentration of graphene quantum dots dispersion, respectively.

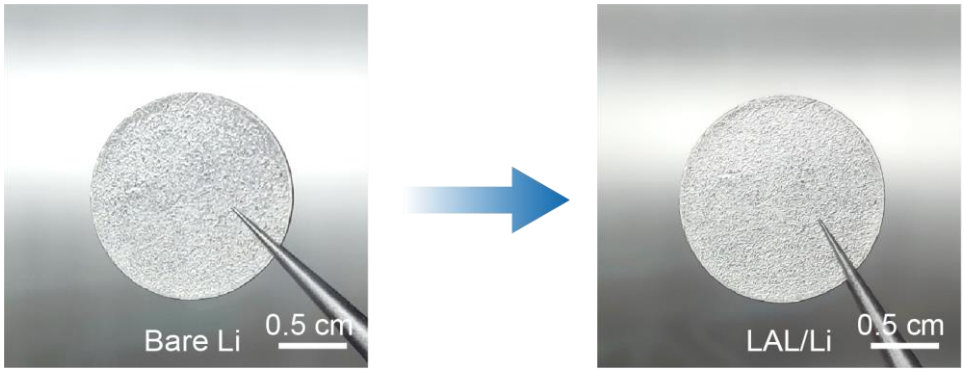

Figure S8. Photographs of the bare Li and the as-prepared LAL/Li electrodes.

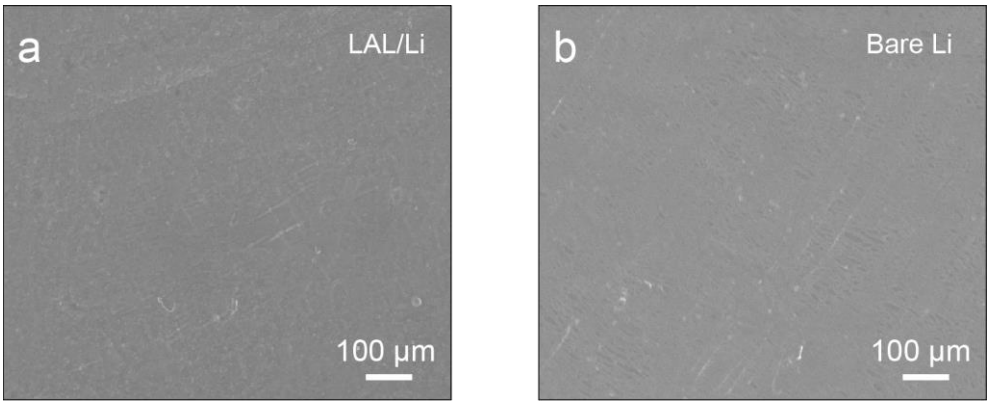

Figure S9. **(a)** and **(b)** SEM images of the as-prepared LAL/Li and bare Li electrodes, respectively.

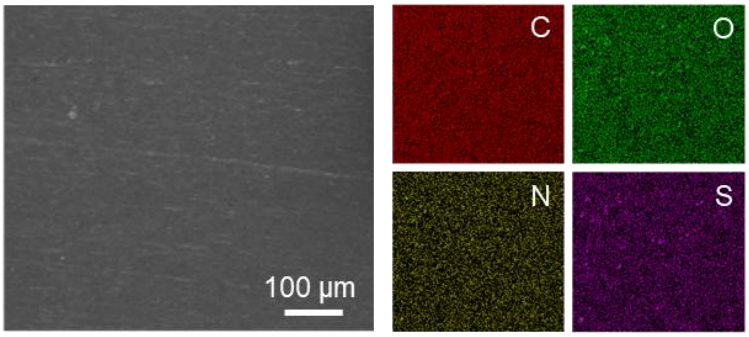

Figure S10. Elemental mappings of the as-prepared LAL/Li electrode.

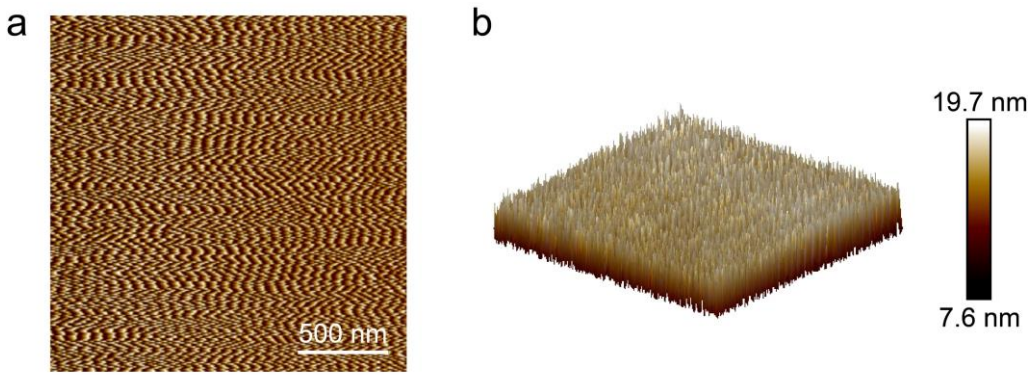

Figure S11. **(a)** and **(b)** The 2D and 3D AFM images of the LAL, respectively.

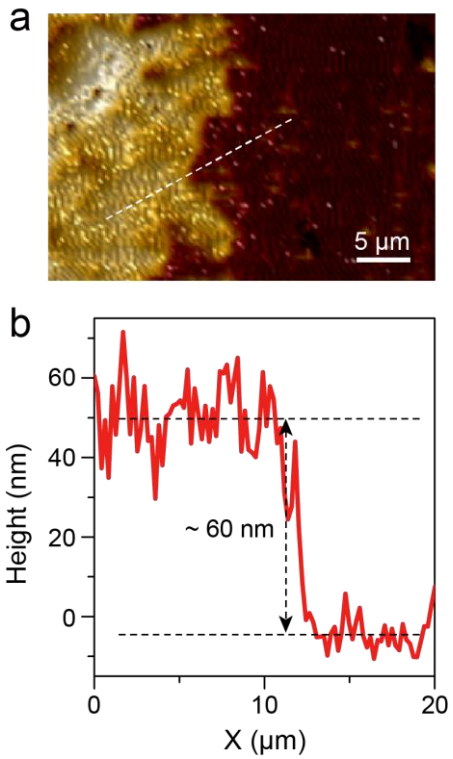

Figure S12. **(a)** AFM topography of the LAL. **(b)** Corresponding thickness profile along the dash line in **a**.

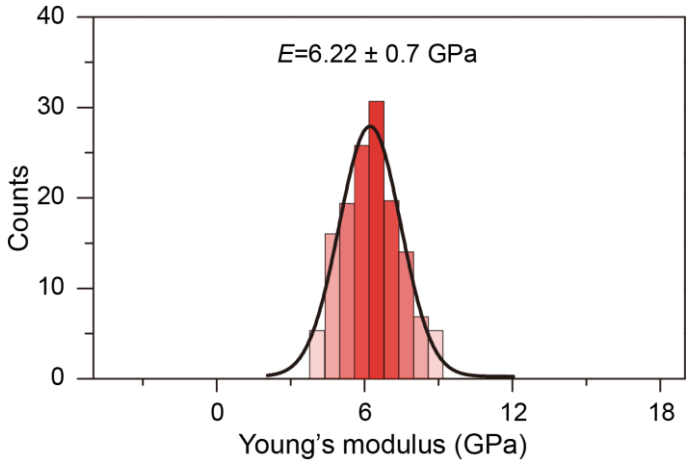

Figure S13. Young's modulus of the LAL obtained by AFM measurement.

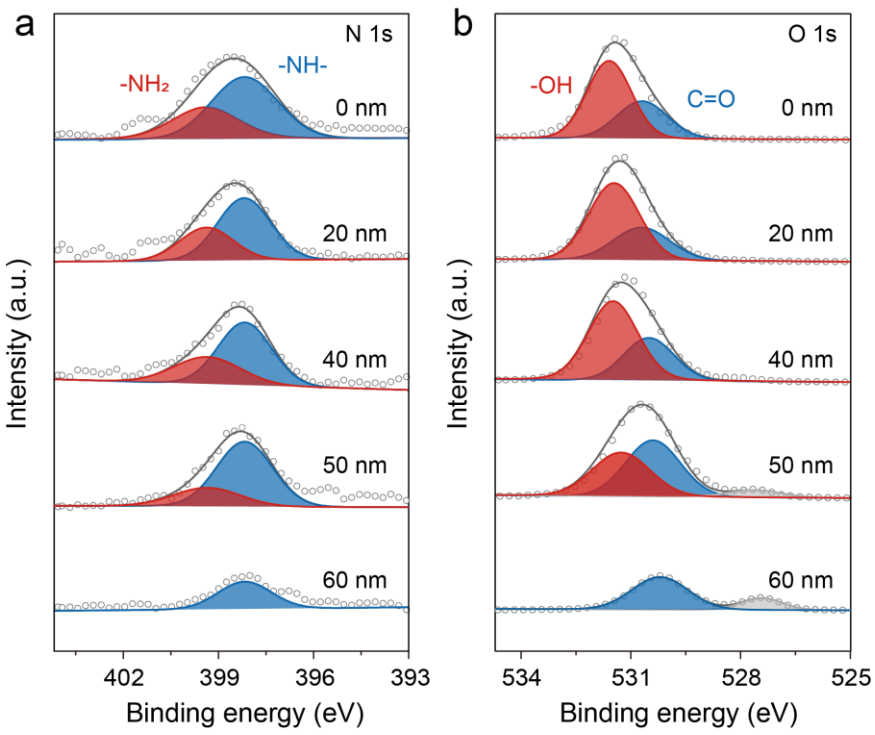

Figure S14. **(a)** and **(b)** XPS depth profiling spectra of the as-prepared LAL/Li electrode. The binding energy values were all calibrated using the adventitious C 1s peak at 284.6 eV.

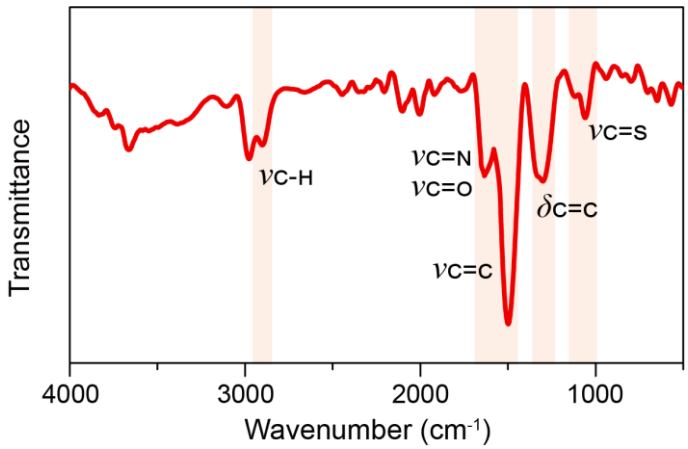

Figure S15. FTIR spectrum of the fully reduced graphene quantum dots by metallic Li.

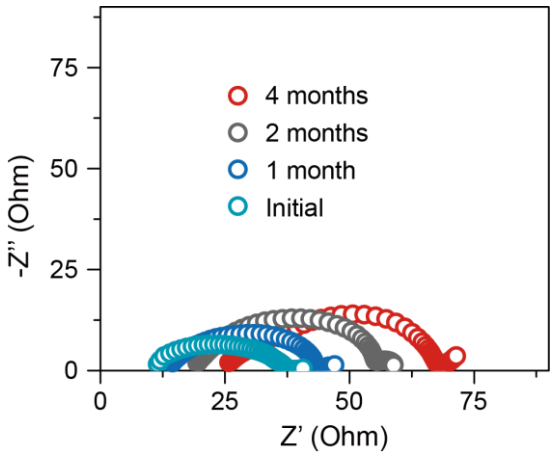

Figure S16. EIS evolution of the symmetric batteries based on LAL/Li electrodes over four months of rest at the open-circuit status.

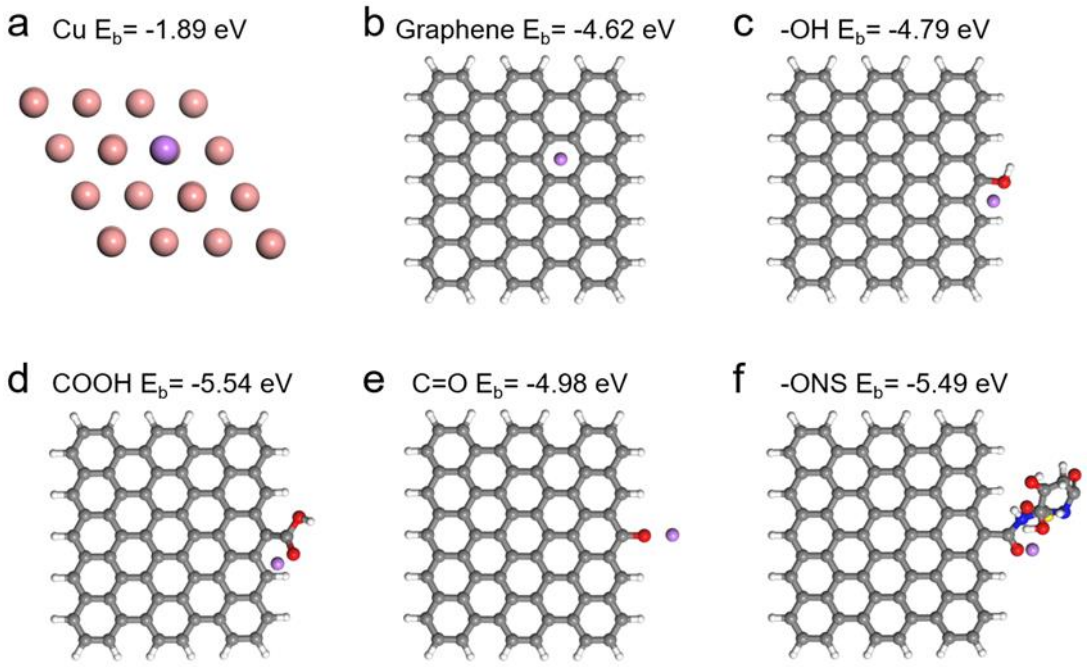

Figure S17. **(a)** Atomic model of Cu used in DFT calculation. **(b)-(f)** Atomic models of graphene quantum dots with different functional groups used in the DFT calculation.

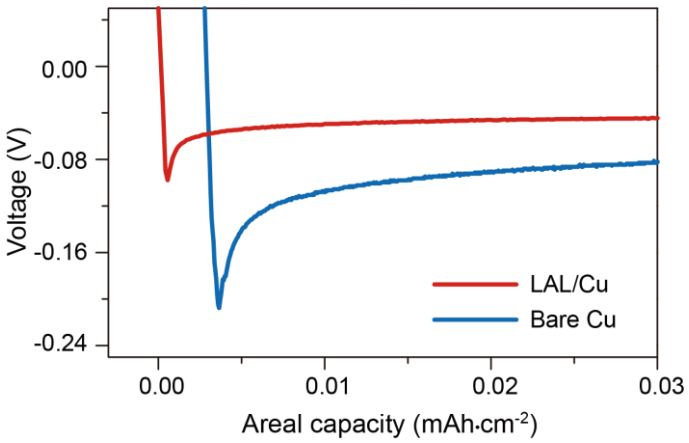

Figure S18. Voltage profiles of Li depositing on the LAL/Cu and bare Cu substrates at 1 mA·cm^{-2}.

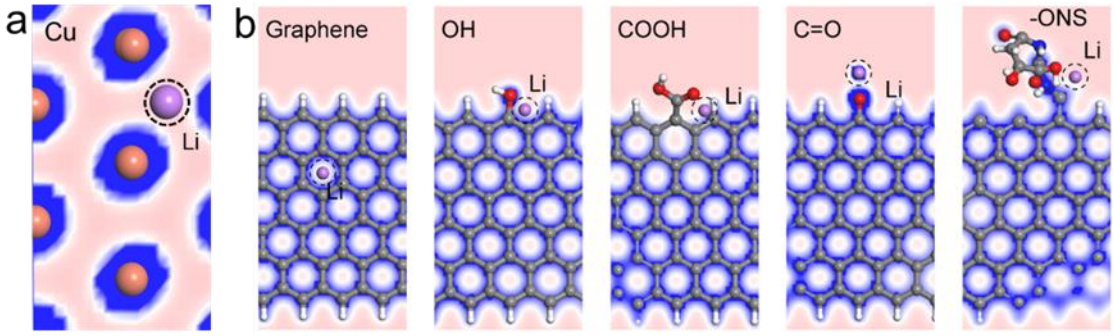

Figure S19. **(a)** and **(b)** Projected charge densities at the Li adsorption sites with Cu and the LAL, respectively.

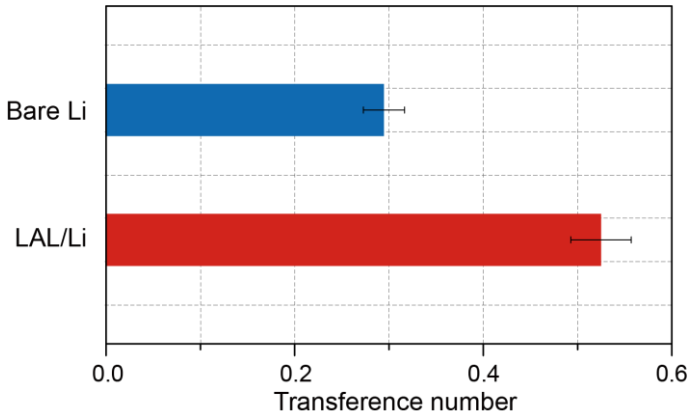

Figure S20. A comparison of Li^+ transference numbers with the LAL/Li and bare Li electrodes.

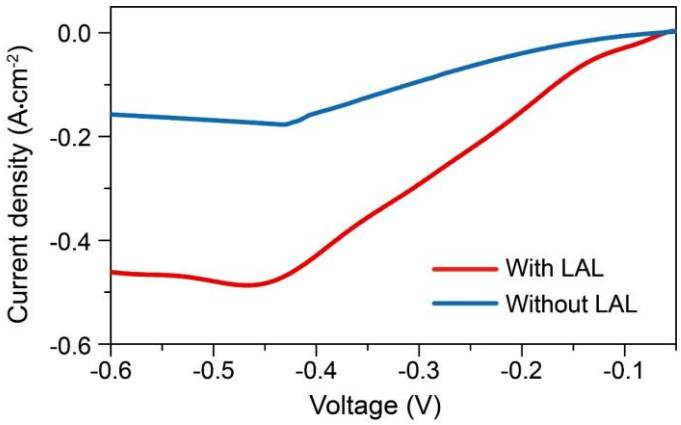

Figure S21. The linear sweep voltammetry of the LAL/Li and bare Li electrodes. Higher diffusion-limited current was obtained with LAL, suggesting a higher local Li^+ concentration and facilitated Li^+ transport.

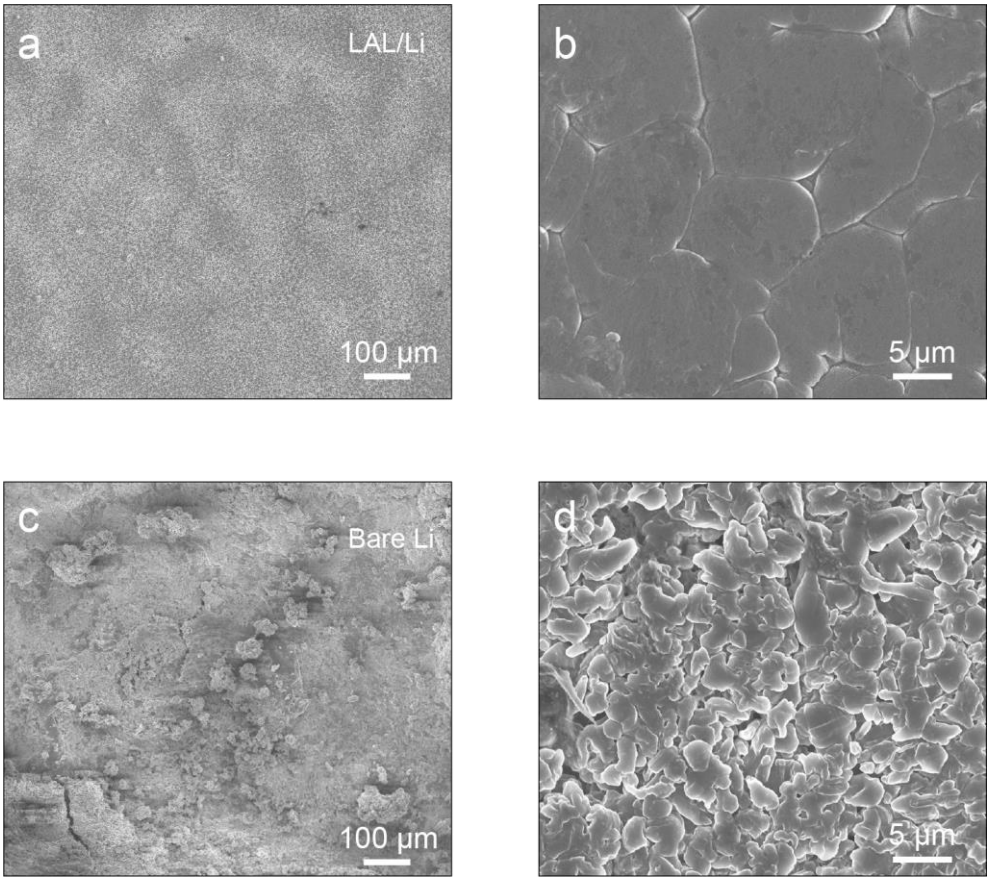

Figure S22. **(a)** and **(b)** Top-view SEM images of the LAL/Li electrode at low and high magnifications, respectively, after 50 cycles at 1 mAh·cm^{-2} and 1 mA·cm^{-2}. **(c)** and **(d)** Top-view SEM images of the bare Li electrode at low and high magnifications, respectively, after 50 cycles at 1 mAh·cm^{-2} and 1 mA·cm^{-2}.

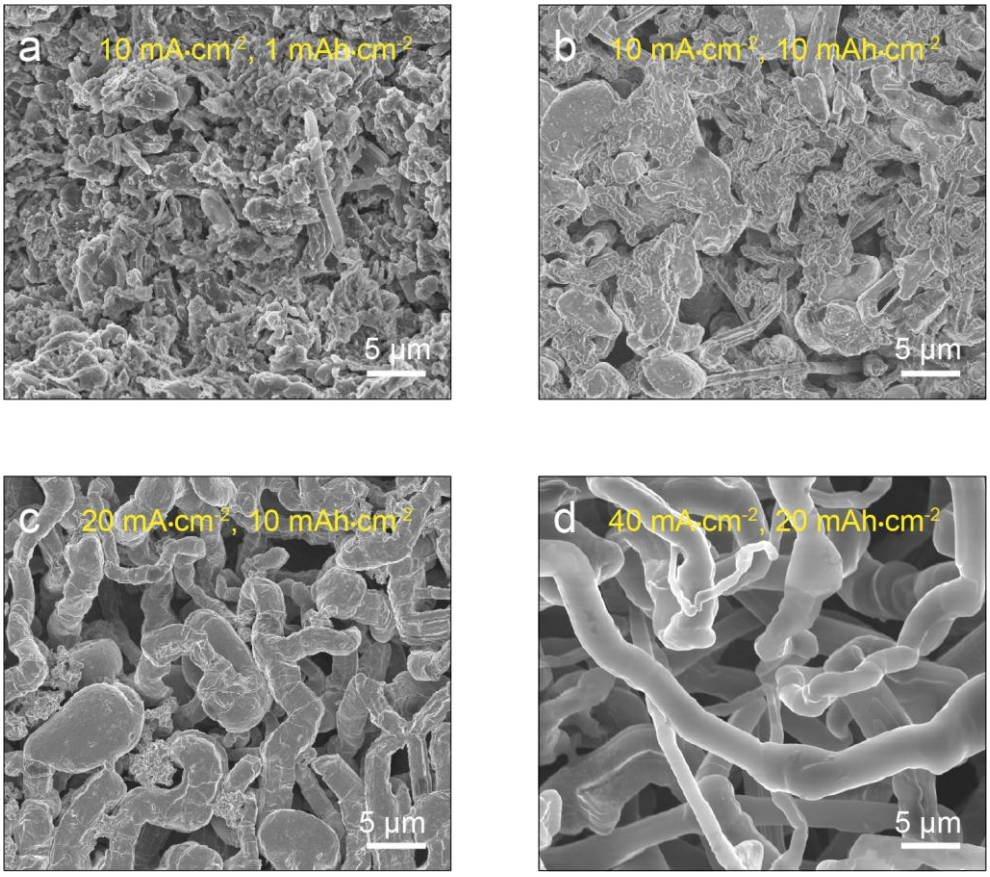

Figure S23. **(a)-(d)** Top-view SEM images of the bare Li electrodes after 50 cycles at conditions including: 1 mAh·cm^{-2} at 10 mA·cm^{-2}, 10 mAh·cm^{-2} at 10 mA·cm^{-2}, 10 mAh·cm^{-2} at 20 mA·cm^{-2}, 20 mAh·cm^{-2} at 40 mA·cm^{-2}, respectively.

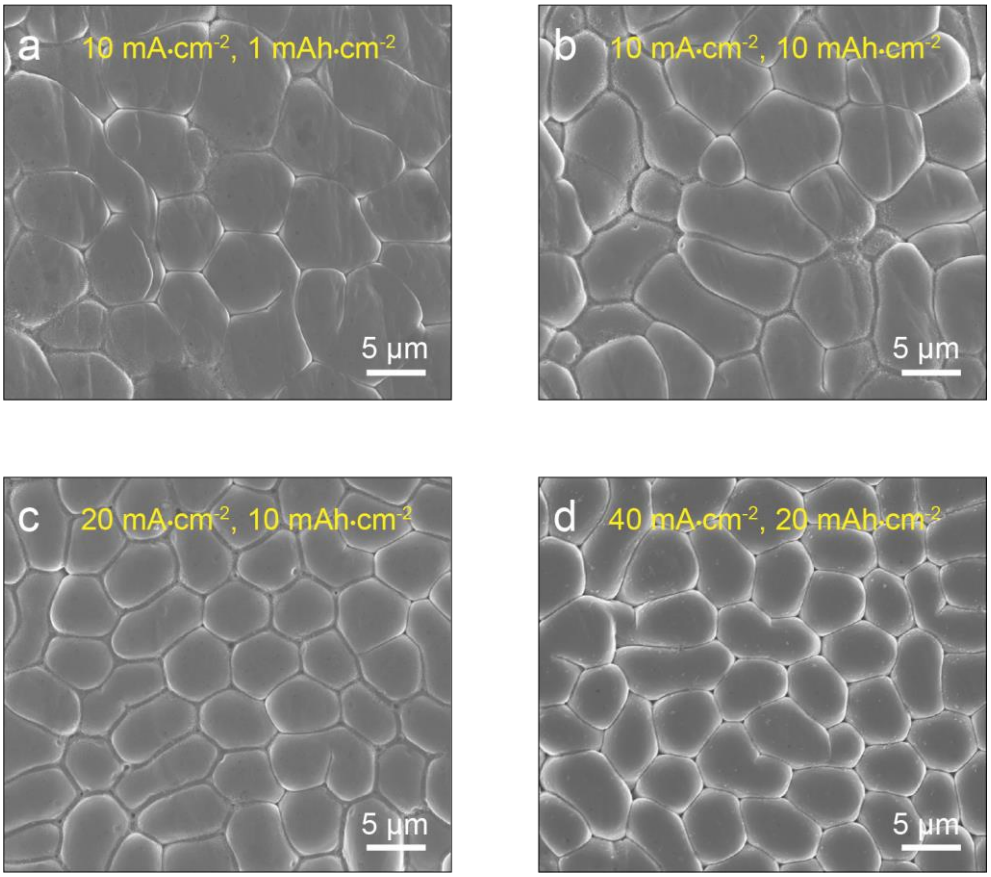

Figure S24. **(a)-(d)** Top-view SEM images of the LAL/Li electrodes after 50 cycles at conditions including: 1 mAh·cm^{-2} at 10 mA·cm^{-2}, 10 mAh·cm^{-2} at 10 mA·cm^{-2}, 10 mAh·cm^{-2} at 20 mA·cm^{-2}, 20 mAh·cm^{-2} at 40 mA·cm^{-2}, respectively.

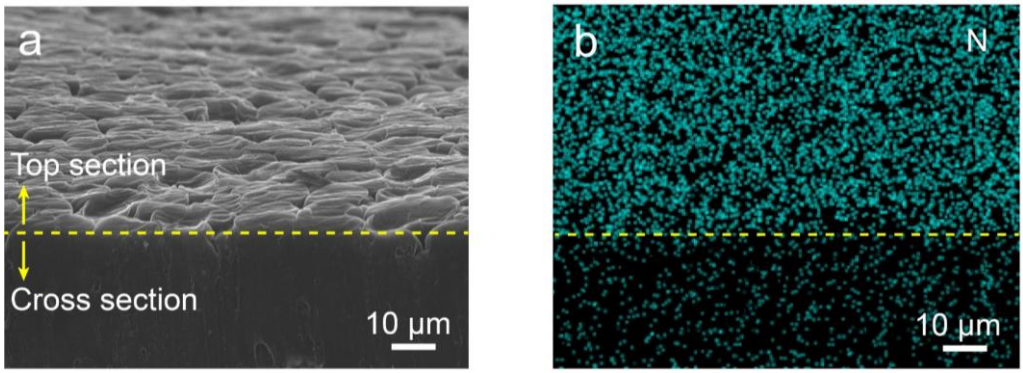

Figure S25. **(a)** and **(b)** SEM image and corresponding nitrogen (N) elemental mapping of the LAL/Li electrode after 50 cycles at 60 mAh·cm^{-2} and 60 mA·cm^{-2}, respectively.

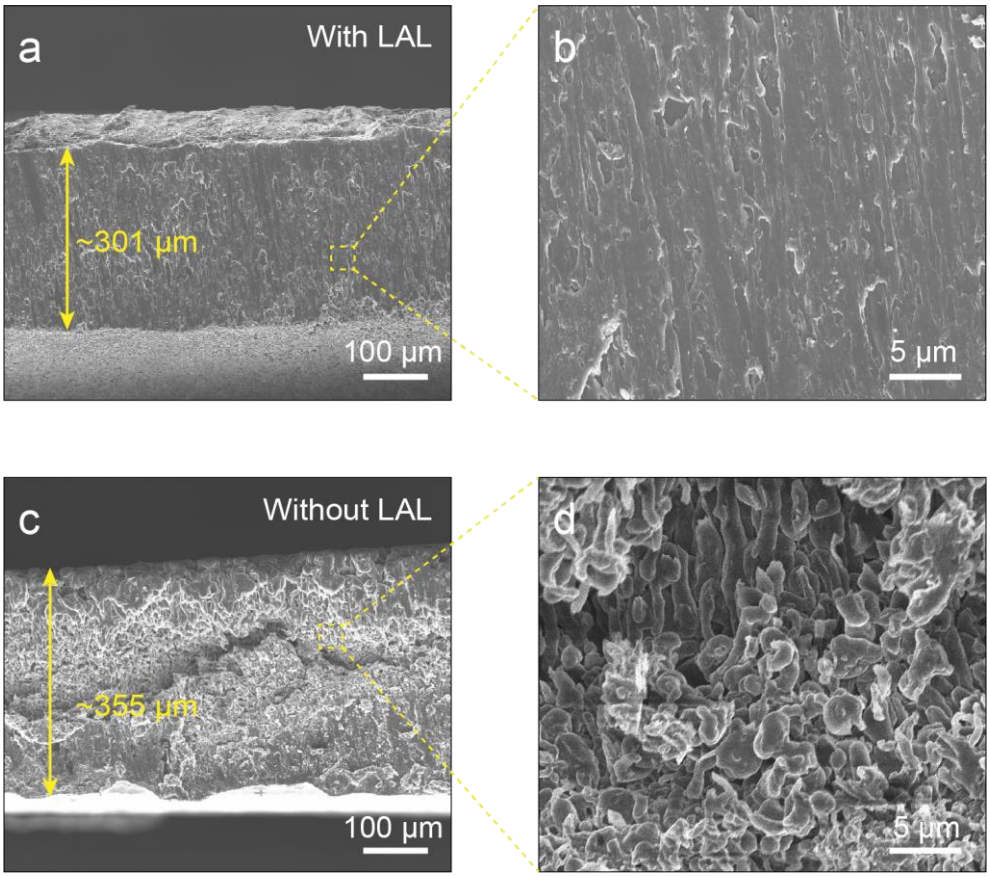

Figure S26. **(a)** and **(b)** Cross-sectional SEM images of the deposited Li on the LAL/Cu substrate with a Li deposition amount of 60 mAh·cm^{-2} at low and high magnifications, respectively. **(c)** and **(d)** The cross-sectional SEM images of the deposited Li on the bare Cu substrate with a Li deposition amount of 60 mAh·cm^{-2} at low and high magnifications, respectively. A current density of 1 mA·cm^{-2} was employed.

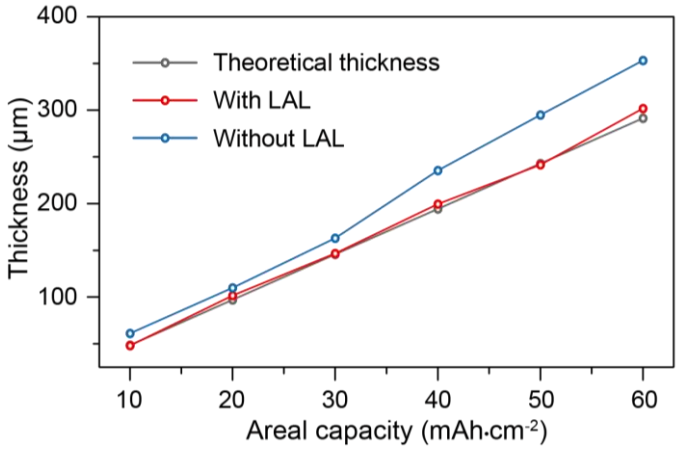

Figure S27. Dependence of deposited Li thickness on Li loading with/without the LAL. A current density of 1 mA·cm^{-2} was employed.

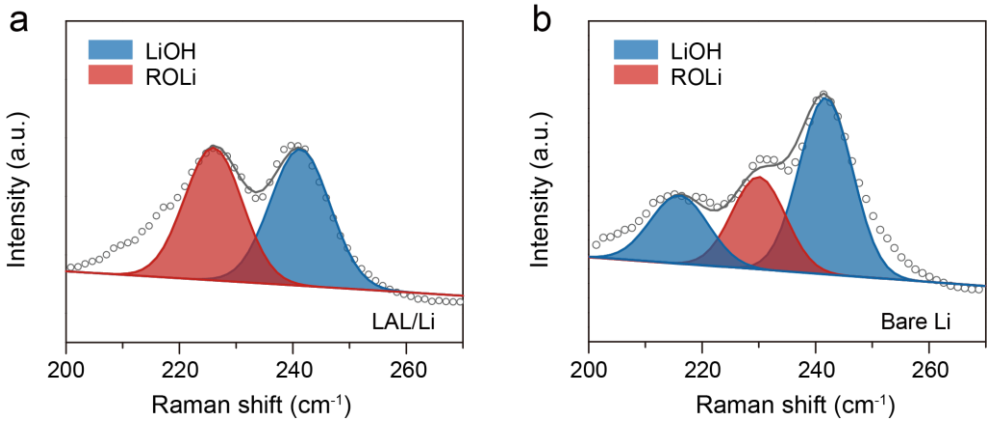

Figure S28. **(a)** and **(b)** Deconvoluted Raman spectra of the signal ranged from 200 to 300 cm^{-1} of the LAL/Li and bare Li electrodes after 50 cycles at 60 $mA \cdot cm^{-2}$ and 60 $mAh \cdot cm^{-2}$, respectively.

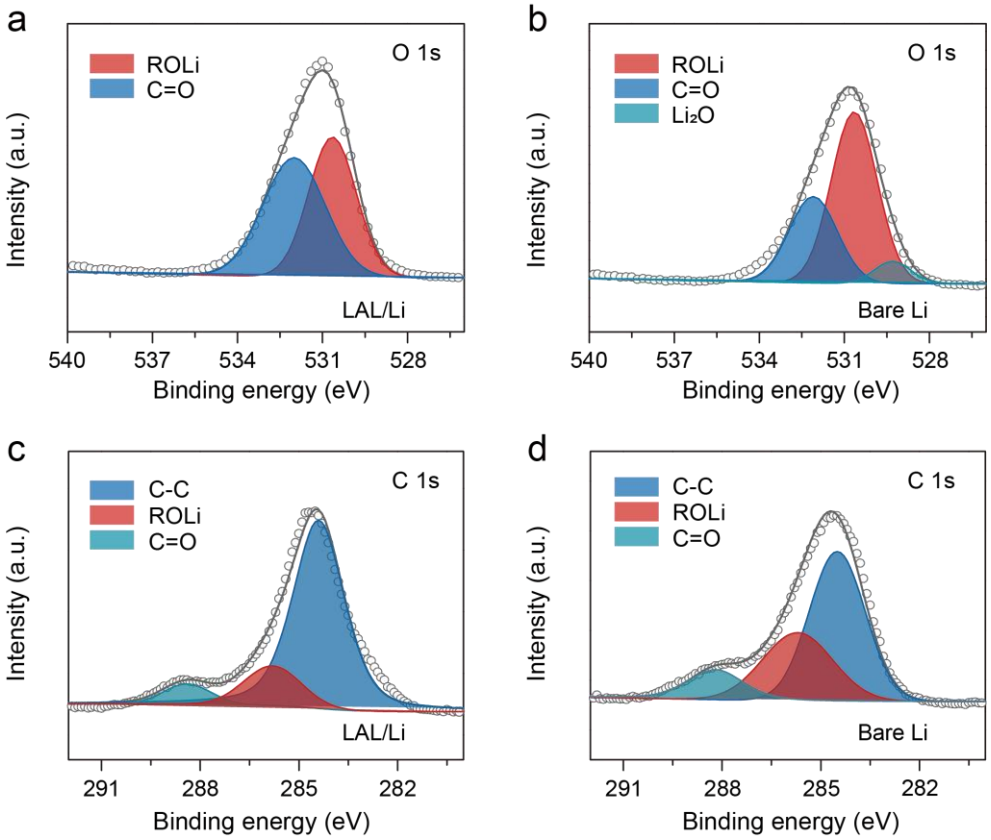

Figure S29. **(a)** and **(b)** High-resolution O 1s XPS spectra of the LAL/Li and bare Li electrodes, respectively, after 50 cycles at 60 mAh·cm^{-2} and 60 mA·cm^{-2}. **(c)** and **(d)** High-resolution C 1s XPS spectra of the LAL/Li and bare Li electrodes, respectively, after 50 cycles at 60 mAh·cm^{-2} and 60 mA·cm^{-2}. The binding energy values were all calibrated using the adventitious C 1s peak at 284.6 eV.

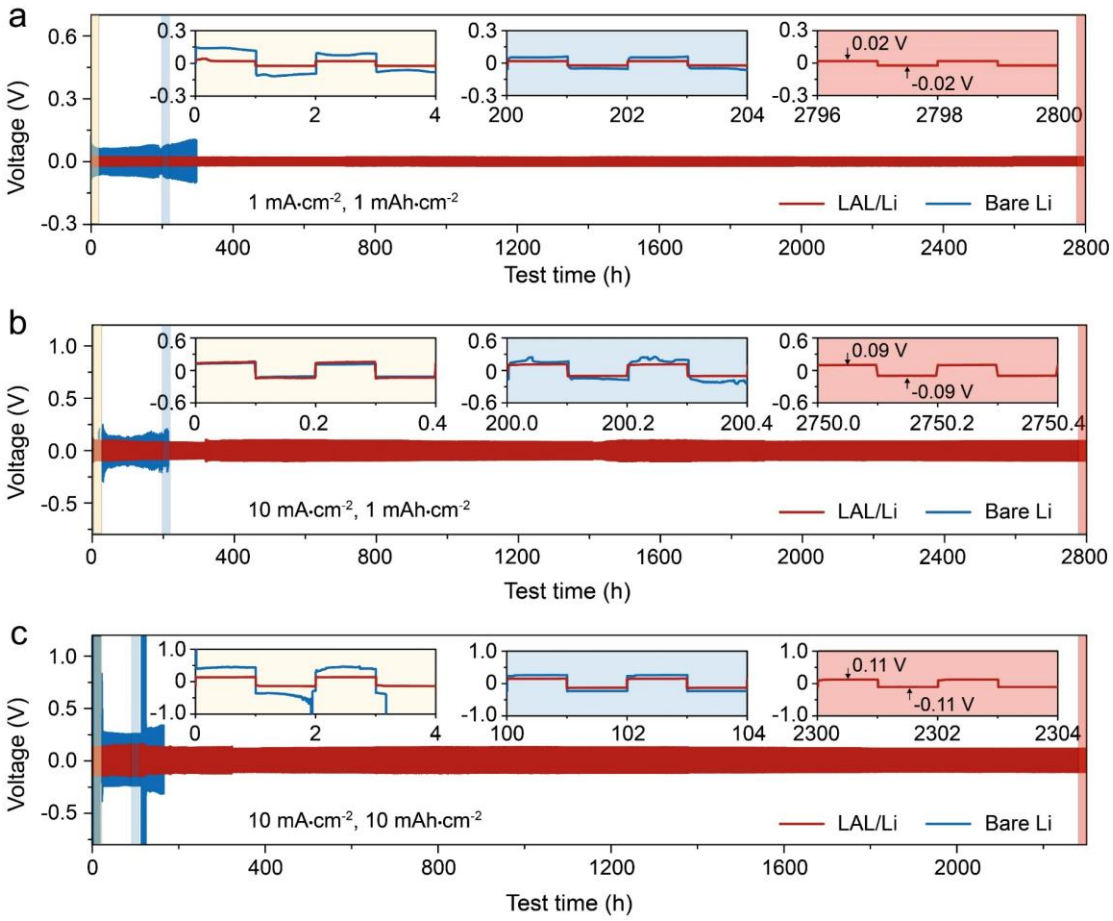

Figure S30. **(a)-(c)** Galvanostatic cycling profiles of symmetric batteries based on LAL/Li and bare Li electrodes, respectively, at cycling conditions including: 1 mAh·cm^{-2} at 1 mA·cm^{-2} **a)**, 1 mAh·cm^{-2} at 10 mA·cm^{-2} **b)**, 10 mAh·cm^{-2} at 10 mA·cm^{-2} **c)**.

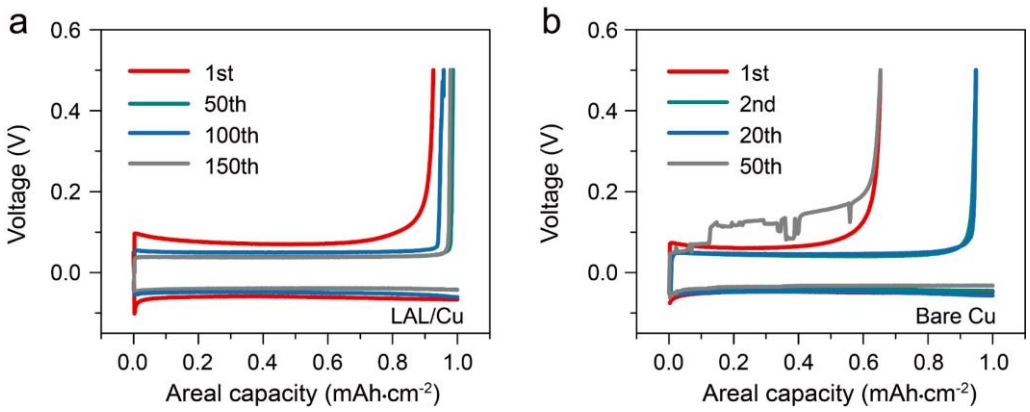

Figure S31. **(a)** and **(b)** Li plating/stripping voltage profiles on the LAL/Cu and bare Cu electrodes, respectively, at 1 mAh·cm^{-2} and 1 mA·cm^{-2}.

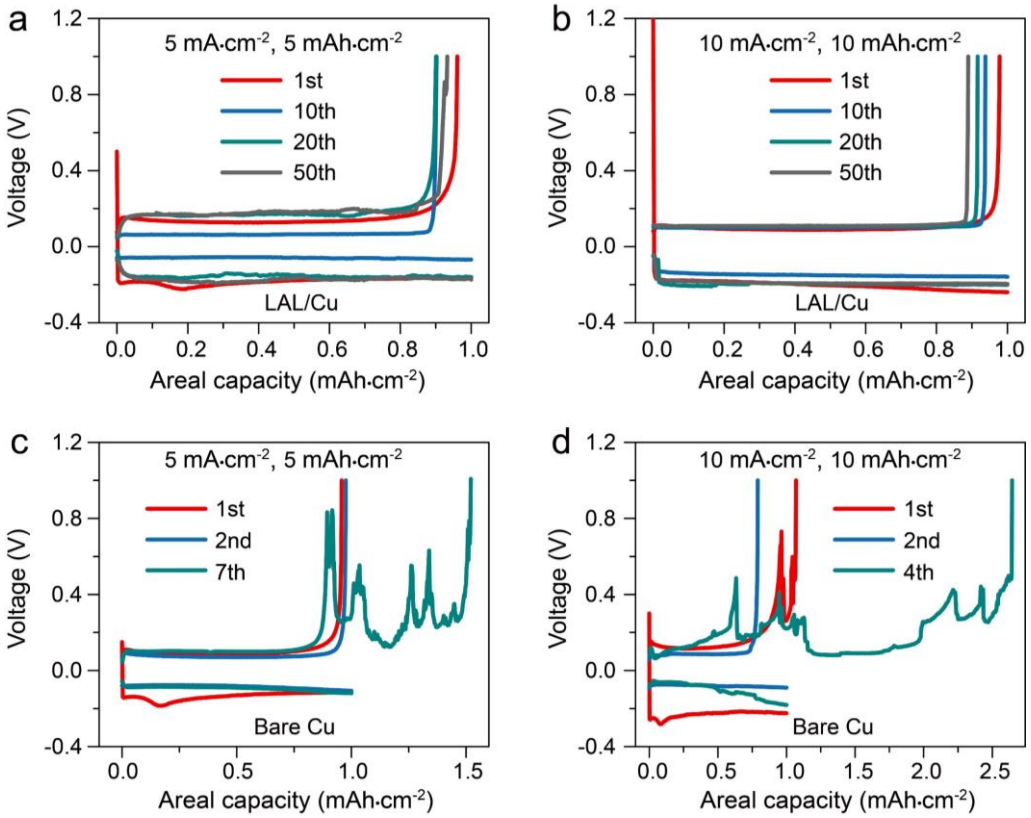

Figure S32. **(a)** and **(b)** Li plating/stripping voltage profiles on the LAL/Cu electrodes at cycling conditions of 5 mAh·cm^{-2} at 5 mA·cm^{-2} and 10 mAh·cm^{-2} at 10 mA·cm^{-2}, respectively. **(c)** and **(d)** Li plating/stripping voltage profiles on the bare Cu electrodes at cycling conditions of 5 mAh·cm^{-2} at 5 mA·cm^{-2} and 10 mAh·cm^{-2} at 10 mA·cm^{-2}, respectively. The batteries were first cycled at 1 mA·cm^{-2} and 1 mAh·cm^{-2} for two cycles to form the initial SEI before cycling at high current density and large capacity.

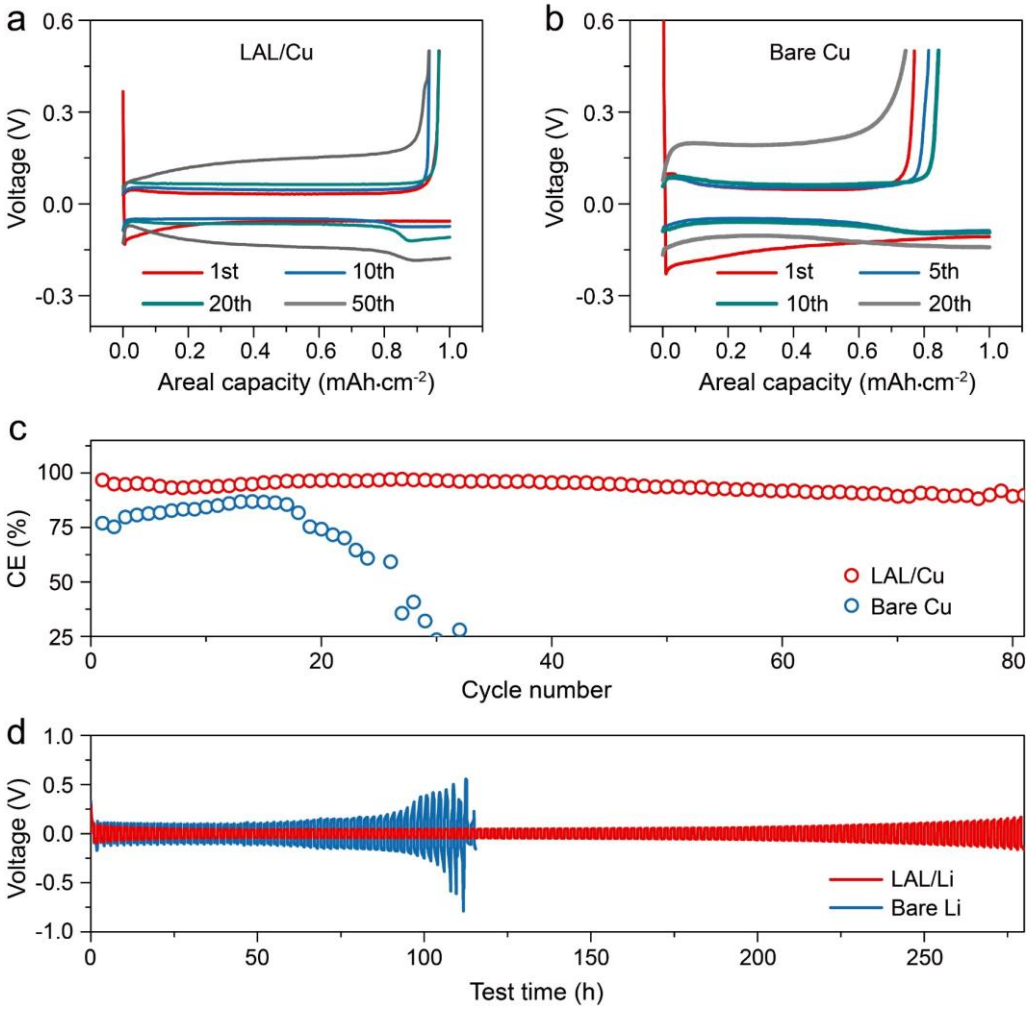

Figure S33. **(a)** and **(b)** Li plating/stripping voltage profiles on the LAL/Cu and bare Cu electrodes at 1 mA·cm^{-2} and 1 mAh·cm^{-2} in commercial carbonate electrolyte of 1 M $LiPF_6$ in EC/DEC (1/1, *v*/*v*). **(c)** Corresponding CEs of the LAL/Cu and bare Cu electrodes. **(d)** Galvanostatic cycling profiles of symmetric batteries of LAL/Li and bare Li electrodes at 1 mA·cm^{-2} and 1 mAh·cm^{-2} in commercial carbonate electrolyte.

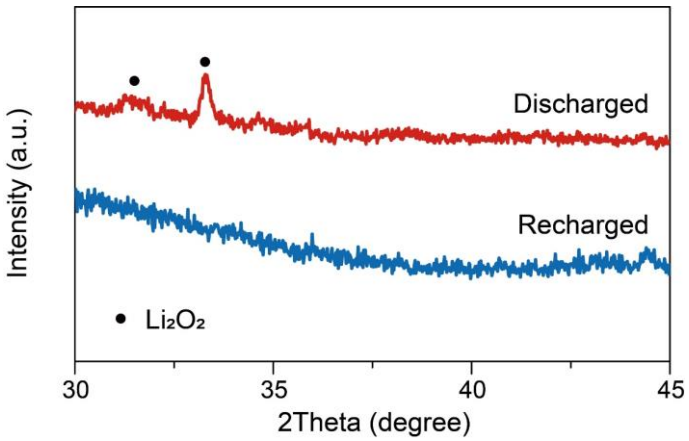

Figure S34. X-ray diffraction (XRD) patterns of the cathode at discharged and recharged states. The peaks in the XRD pattern after discharge were assigned to Li_2O_2.

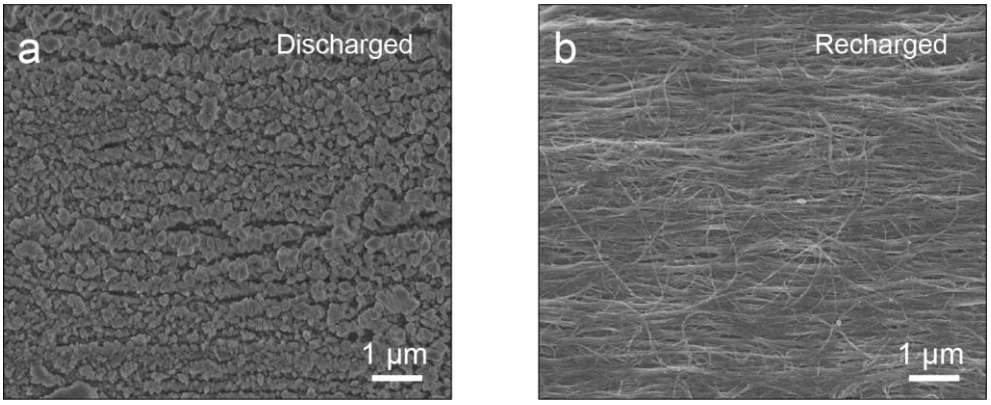

Figure S35. **(a)** and **(b)** SEM images of the CNT cathode after discharge and recharge, respectively.

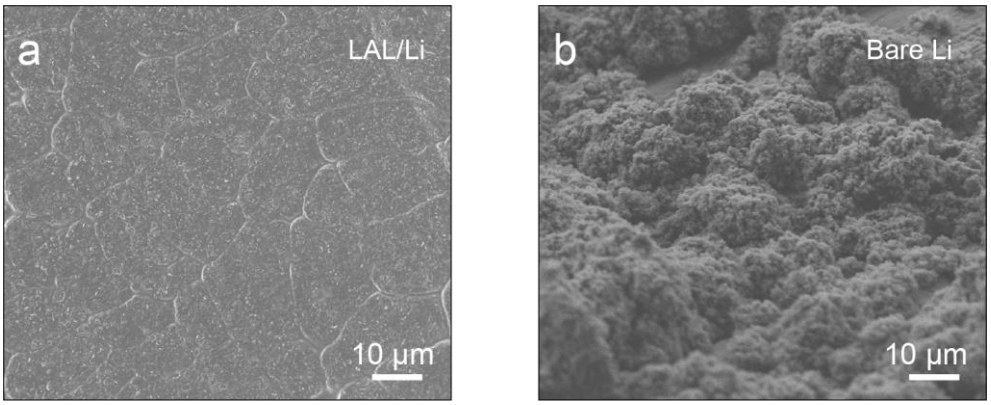

Figure S36. **(a)** and **(b)** SEM images of the LAL/Li and bare Li anodes, respectively, after 50 cycles in Li-air batteries at 1000 $mA \cdot g^{-1}$ and 500 $mAh \cdot g^{-1}$.

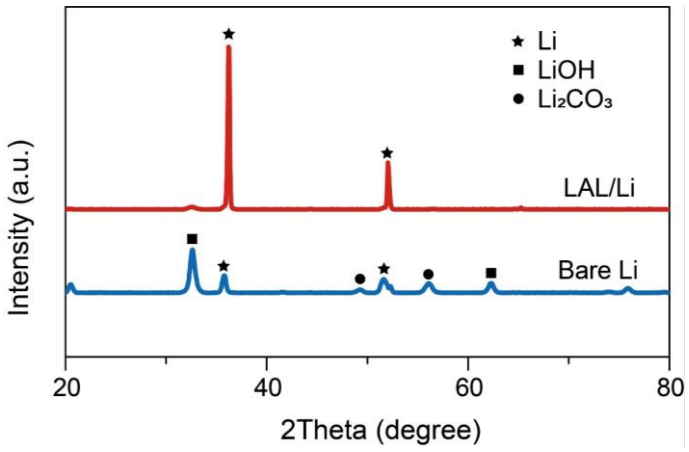

Figure S37. XRD patterns of the LAL/Li and bare Li anodes after 50 cycles (1000 $mA \cdot g^{-1}$ and 500 $mAh \cdot g^{-1}$) in Li-air batteries.

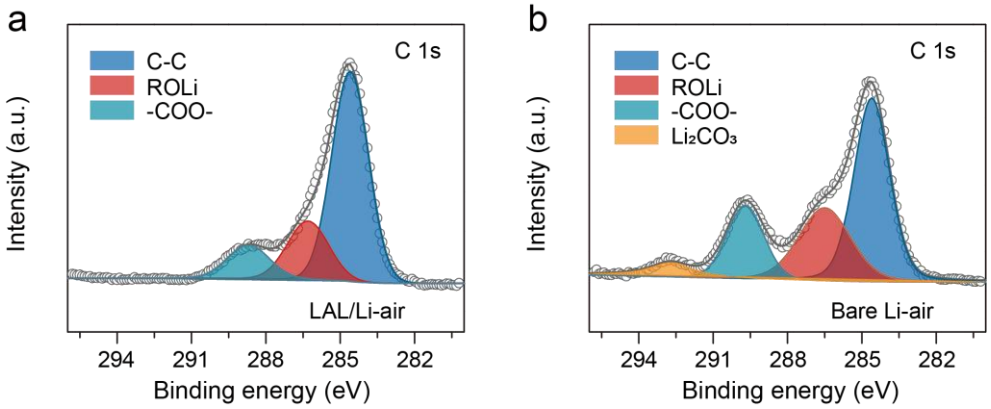

Figure S38. **(a)** and **(b)** High-resolution C 1s spectra of the LAL/Li and bare Li anodes after 50 cycles (1000 $mA \cdot g^{-1}$ and 500 $mAh \cdot g^{-1}$) in Li-air batteries, respectively.

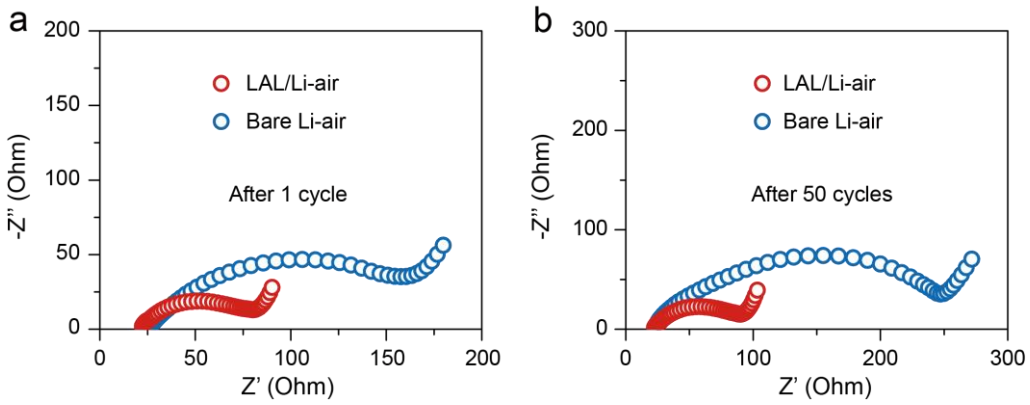

Figure S39. **(a)** and **(b)** Nyquist plots of the Li-air batteries based on the LAL/Li and bare Li anodes after the initial and 50 cycles (1000 $mA \cdot g^{-1}$ and 500 $mAh \cdot g^{-1}$), respectively.

Table S1. The Li^+ adsorbing effect of the LAL in electrolyte.

Electrolyte		Concentration (Li^+, $mol \cdot L^{-1}$)	Volume (mL)
Before treatment with LAL		0.6689	1.9
After treated with LAL	Top	0.6559	1.4
	Bottom (with LAL)	0.6889	0.5

30 mg graphene quantum dots were immersed in 1.9 mL electrolyte for 3 days in a tube with high aspect ratio. Then 1.4 mL top layer and 0.5 mL bottom layer of the treated electrolyte were collected for inductively coupled plasma (ICP) analysis. The obtained Li^+ concentration was lower than the supposed 1 M, due to the mass loss during pretreatment of the electrolyte before ICP analysis. It included solvent evaporation, dry ablation and nitric acid nitration to remove the organic compound in electrolyte before ICP analysis.

Table S2. Comparison of the areal capacity, current density, and cycle performance of this work and previously reported excellent Li metal anodes.

Ref	Strategy	Areal capacity ($mAh \cdot cm^{-2}$)	Current density ($mA \cdot cm^{-2}$)	Cycling time (h)
This work	**Li^+ adsorbing layer**	**10**	**20**	**1900**
		20	**40**	**1200**
		60	**60**	**1100**
3	TPFPB and $LiNO_3$ additives	3	1.5	400
4	Tin (II) additive	3	1	900
5	NaTFSI additive	1	1	1200
6	Self-healable polymer electrolyte	1	1	200
7	Hierarchical polymer electrolyte	3	1	480
8	MXene ($Ti_3C_2T_x$) layer	35	1	420
9	Polymer-inorganic layer	4	2	1200
10	LiPEO-UPy layer	10	5	1000
11	PTMEG-Li/Sn	1	1	1000
12	Deposition-regulating scaffold	3.5	10	60
13	CNT sponge	2	40	20
14	Cu_3N-3D Cu	1	20	120

Table S3. Fitted EIS results for LAL/Li and bare Li electrodes in symmetric batteries.

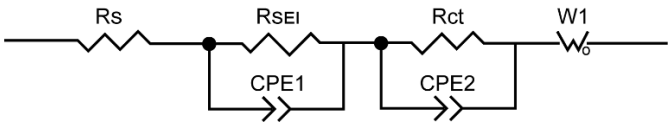

Cycles	R_s (Ω)		R_{SEI} (Ω)		R_{ct} (Ω)	
	LAL/Li	**Bare Li**	**LAL/Li**	**Bare Li**	**LAL/Li**	**Bare Li**
1 cycle	11	11.3	15	10	33.9	48
50 cycles	6	12.1	16	38.2	31	85.8

R_s, R_{SEI}, and R_{ct} represented electrolyte resistance, interfacial resistance, and charge transfer resistance, respectively.

References for the Supporting Information

[1] B. Delley, *J. Chem. Phys.* **2000**, *113*, 7756-7764.

[2] J. Perdew, K. Burke, M. Ernzerhof, *Phys. Rev. Lett.* **1996**, *77*, 3865-3868.

[3] S. Li, W. Zhang, Q. Wu, L. Fan, X. Wang, X. Wang, Z. Shen, Y. He, Y. Lu, *Angew. Chem. Int. Ed.* **2020**, *59*, 14935-14941.

[4] W. Zhang, Q. Wu, J. Huang, L. Fan, Z. Shen, Y. He, Q. Feng, G. Zhu, Y. Lu, *Adv. Mater.* **2020**, *32*, 2001740.

[5] H. Sun, G. Zhu, Y. Zhu, M. Lin, H. Chen, Y. Li, W. Hung, B. Zhou, X. Wang, Y. Bai, M. Gu, C. Huang, H. Tai, X. Xu, M. Angell, J. Shyue, H. Dai, *Adv. Mater.* **2020**, *32*, 2001741.

[6] N. Wu, Y. Shi, S. Lang, J. Zhou, J. Liang, W. Wang, S. Tan, Y. Yin, R. Wen, Y. Guo, *Angew. Chem. Int. Ed.* **2019**, *58*, 18146-18149.

[7] D. Zhou, A. Tkacheva, X. Tang, B. Sun, D. Shanmukaraj, P. Li, F. Zhang, M. Armand, G. Wang, *Angew. Chem. Int. Ed.* **2019**, *58*, 6001-6006.

[8] D. Zhang, S. Wang, B. Li, Y. Gong, S. Yang, *Adv. Mater.* **2019**, *31*, 1901820.

[9] Y. Gao, Z. Yan, J. Gray, X. He, D. Wang, T. Chen, Q. Huang, Y. C. Li, H. Wang, S. Kim, T. Mallouk, D. Wang, *Nat. Mater.* **2019**, *18*, 384-389.

[10] G. Wang, C. Chen, Y. Chen, X. Kang, C. Yang, F. Wang, Y. Liu, X. Xiong, *Angew. Chem. Int. Ed.* **2020**, *59*, 2055-2060.

[11] Z. Jiang, L. Jin, Z. Han, W. Hu, Z. Zeng, Y. Sun, J. Xie, *Angew. Chem. Int. Ed.* **2019**, *58*, 11374-11378.

[12] J. Pu, J. Li, K. Zhang, T. Zhang, C. Li, H. Ma, J. Zhu, P. Braun, J. Lu, H. Zhang, *Nat. Commun.* **2019**, *10*, 1896.

[13] Z. Wang, Z. Lu, W. Guo, Q. Luo, Y. Yin, X. Liu, Y. Li, B. Xia, Z. Wu, *Adv. Mater.* **2021**, *33*, 2006702.

[14] Z. Li, Q. He, C. Zhou, Y. Li, Z. Liu, X. Hong, X. Xu, Y. Zhao, L. Mai, *Energy Storage Mater*. **2021**, *37*, 40-46.